



# Multidisciplinary design optimization of a dual-spin guided vehicle

Jalal Karimi\*, Mohammad Reza Rajabi, Seyed Hossein Sadati, Seyed Mahid Hosseini

Department of Aerospace Engineering, Malek Ashtar University of Technology, Tehran, Iran

## ARTICLE INFO

### Article history:

Received 6 March 2023

Received in revised form

22 July 2023

Accepted 22 November 2023

Available online 29 November 2023

### Keywords:

Flying projectile optimal design

All-at-ones multidisciplinary optimization

Structure discipline

Guidance and control discipline

Aerodynamic discipline

## ABSTRACT

In this research, a Multidisciplinary Design Optimization approach is proposed for the dual-spin guided flying projectile design considering external and internal parts of the body as design variables. In this way, a parametric formulation is developed. All related disciplines, including structure, aerodynamics, guidance, and control are considered. Minimum total mass, maximum aerodynamic control effectiveness, minimum miss distance, maximum yield stress in all subsystems, controllability and gyroscopic stability constraints are some of objectives/constraints taken into account. The problem is formulated in All-At-Ones Multidisciplinary Design Optimization approach structure and solved by Simulated Annealing and minimax algorithms. The optimal configurations are evaluated in various aspects. The resulted optimal configurations have met all design objectives and constraints.

© 2023 China Ordnance Society. Publishing services by Elsevier B.V. on behalf of KeAi Communications Co. Ltd. This is an open access article under the CC BY-NC-ND license (<http://creativecommons.org/licenses/by-nc-nd/4.0/>).

## 1. Introduction

Unguided spin-stabilized projectiles suffer from significant errors in hitting the targets. These projectiles are intended to be converted to guided flying vehicles. Guidance and control of spin-stabilized vehicles poses challenges due to limitations in actuators, navigation sensors, and guidance sensors when dealing with high roll rates. One possible solution of this problem is to use the dual-spin configuration. The dual-spin configuration concept benefits from advantages of both spin-stabilized and fin-stabilized airframes at the same time. Similar to that of spin-stabilized airframes, the gyroscopic stability benefits are utilized by keeping the aft body high roll rate. On the other hands, fin-stabilized airframes or vehicles with small roll rates make it possible to use low-cost sensors for guidance and navigation. In addition, non-rolling airframes provide a better performance in guidance and reaching the target, rather than rolling airframes. In dual-spin configuration, the vehicle's body is divided into two sections: the fore-body and the aft-body. The fore-body maintains a low roll rate, while the aft-body spins freely at a high roll rate to maintain gyroscopic stability. The flight control unit is located in the fore-body, allowing for navigation and control similar to fin-stabilized vehicles. Fig. 1 shows a typical dual-spin configuration.

Dual-spin configurations are assessed in various research studies. The dynamic model of dual-spin vehicles has been developed in some researches [1–4]. Stability characteristics and linearization of dynamic model were addressed in Refs. [4–12] using Linear Parameter Varying (LPV) and quasi-LPV (q-LPV) methods. Control methods such as feedback-linearization and fixed canard angle approach are proposed in Refs. [13–19].

Various disciplines have been used for optimal design of flying vehicles. The design objectives of range, aerodynamic efficiency, mass, miss distance, and fuel consumption are used in Refs. [20,21]. Refs. [22–26] have used aerodynamics, propulsion, mass, and trajectory disciplines for optimizing the configuration and geometry of a missile. In optimal design of a dual-spin projectile, also, various disciplines of structure, aerodynamics, guidance and control must be handled simultaneously, to get an appropriate configuration. Therefore, one can claim that this problem is inherently a Multidisciplinary design Optimization (MDO) problem.

MDO approaches have been used in designing modern engineering systems with optimal performance, especially aerospace systems [27,28]. The classified MDO algorithms into single-level and multi-level algorithms applied in Refs. [29–31]. Single-level algorithms solve the optimization problem by determining design variables only. Meanwhile, in multi-level algorithms, the multi-discipline optimizers are used to determine discipline variables, and the synchronous system-level optimizer calculates the variables shared between disciplines. The most common MDO algorithms are collaborative optimization [28,31–33], concurrent sub-

\* Corresponding author.

E-mail address: [karimi\\_j@mut.ac.ir](mailto:karimi_j@mut.ac.ir) (J. Karimi).

Peer review under responsibility of China Ordnance Society

**Nomenclature**

$C_A$	The axial aerodynamic force
$C_Y$	The Side Force of coefficient is derivative with the sideslip angle
$C_{Yp\alpha}, C_{Yp\beta}$	Magnus coefficient due to angle of $\alpha$ or $\beta$
$C_{Yp\alpha}^a$	Side-force Coefficient change about to Roll rate and Sideslip Angle in aft body
$C_{Yp\alpha}^f$	Side-force Coefficient change about to Roll rate and Sideslip Angle in forward body
$C_{Y\dot{\beta}}$	Side-force Coefficient change with regard to Sideslip Angle rate
$C_{Y\dot{\delta}_r}$	Side-force Coefficient change with regard to canard angle in yaw channel
$C_m$	Pitching Moment coefficient
$C_{mp\alpha}^a$	$C_{mp\alpha}^a$ Pitching Moment Coefficient change concerns Roll Rate and angle of attack in the forward and aft body. (Magnus moment)
$C_N, C_{N\beta}$	Normal Force Coefficient
$C_n$	Yawing Moment Coefficient
$I$	Inertial moment matrix
$I_x$	Main axial inertial moment of each component
$I_y$	Main lateral inertial moment of each component
$X_{Cgt}$	Total center of gravity of vehicle
$X_{Cg}$	Center of gravity in each subsystem
$m_t$	Vehicle total mass
$S_G$	Gyroscopic stability factor for rotary vehicles
$S_D$	Dynamic stability factor for rotary vehicles

$\delta_{a,r,e}(i)$	Aileron, elevator and rudder deflection in
$Cn_{p\beta}^f, Cn_{p\beta}^a$	Yawing Moment Coefficient changes with regard to Roll Rate and angle of Sideslip in the forward and body
$C_{Np\alpha}^f, C_{Np\alpha}^a$	Magnus force aerodynamic coefficient for the forward and aft bodies
$Cn_r$	The Yawing Moment Coefficient derivative with yaw rate
$Cn_{\dot{\beta}}$	The Yawing Moment Coefficient derivative with the rate of change Sideslip angle (body axis)
$(\varphi, \theta, \psi)$	Vehicle Euler angles
$\dot{\varphi}_f$	The rate of $\varphi$ in forward body
$\dot{\varphi}_a$	The rate of $\varphi$ in aft body
$\dot{\theta}$	The rate of $\theta$ in total body
$m_d$	Miss Distance
$c_e$	Control effort parameter
$(p, q, r)$	Vehicle angular velocity components
$(u, v, w)$	Vehicle velocity components
$D_{ref}, D, d$	Vehicle caliber
$S_{ref}$	The surface reference of the vehicle
$\sigma_L$	Longitudinal stress in bottom of each section
$\sigma_{Axial}$	Axial stress in each sections
$n$	Number of time steps in simulation

**Abbreviations**

AAO	All-At-Ones Multidisciplinary Optimization
SA	Simulated Annealing

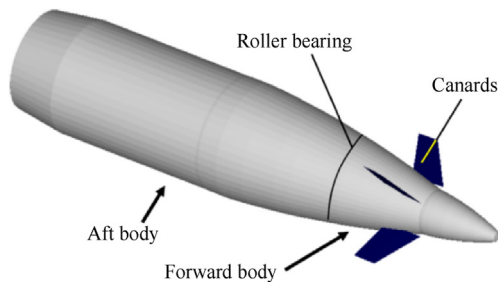


Fig. 1. Dual-spin configuration with canard control surfaces.

space optimization [34], bi-level integrated system synthesis [35,36], analytical target cascading [37,38], multiple discipline feasible [39], and All-At-Ones (AAO) [40].

Several optimization algorithms such as evolutionary algorithms [24,41–43], Simulated Annealing (SA) [44], hybrid search [45], and evolutionary algorithms have been used for optimal configuration design. Refs. [46,47] improve the upper-stage multidisciplinary optimization design process using the combined framework algorithms and MSDO (Multidisciplinary system design optimization) algorithm in tandem. Ref. [48] improved the automated design optimization routine and used it for aerodynamic shape optimization designing of long range guided projectile fires.

As previously mentioned, the objective of the current research is to enhance an existing unguided vehicle by converting it into a guided dual-spin vehicle. This requires adding a flight control unit and redesigning all internal and external parts of the body. In this way, all design disciplines including structural, aerodynamic, stability, control, and internal layout design are taken into account. A

novel parametric formulation is developed for all disciplines to make them suitable for the optimization problem. All disciplines are integrated into an MDO problem based on the AAO algorithm and solved using SA and minimax algorithms.

**2. AAO algorithm**

The AAO algorithm is a simplified version of the multiple discipline feasible algorithm that aims to reduce the number of evaluations. Although the AAO algorithm takes additional time to converge, it provides more accurate compute decompositions [49]. In this approach, a design vector value is deemed acceptable only if all constraints are satisfied. The AAO algorithm treats the MDO problem as a single optimization problem and evaluates all disciplines simultaneously. The formulation of the AAO method for a MDO problem with  $N$  disciplines is presented in Eq. (1), [50,51].

$$\text{minimize: } f_0(\mathbf{x}, \mathbf{y}) + \sum_{i=0}^N f_i(\mathbf{x}_0, \mathbf{x}_i, \mathbf{y}_i)$$

with respect to  $\mathbf{x}, \hat{\mathbf{y}}, \mathbf{y}$

$$\text{subject to } \mathbf{c}_0(\mathbf{x}_0, \mathbf{y}) \geq 0 \quad (1)$$

$$\mathbf{c}_i(\mathbf{x}_0, \mathbf{x}_i, \mathbf{y}_i) \geq 0 \text{ for } i = 1, 2, \dots, N$$

$$\mathbf{c}_i^e(\hat{\mathbf{y}}_i, \mathbf{y}_i) = \hat{\mathbf{y}}_i - \mathbf{y}_i = 0 \text{ for } i = 1, 2, \dots, N$$

$$\mathbf{R}_i(\mathbf{x}_0, \mathbf{x}_i, \hat{\mathbf{y}}_i, \mathbf{y}_i) = 0 \text{ for } i = 1, 2, \dots, N$$

where  $\mathbf{x}$  denotes vector of design variables,  $\mathbf{x}_0$  is vector of shared variables, and  $\mathbf{x}_i$  denotes vector of variables local to discipline  $i$ . The set of equations governing discipline analysis  $i$  is denoted by  $\mathbf{R}_i$ , and the corresponding set of state variables is denoted by  $\mathbf{y}_i$ . The set of

state variables computed by all disciplines is denoted by  $\mathbf{y}$ , and the number of disciplines is denoted by  $N$ . The letters  $\mathbf{f}_0$  and  $\mathbf{f}_i$  are shared design objectives, and shared design objective for the  $i$ th discipline objective of the MDO problem, respectively. The coupling variables are denoted by the same symbol as the state variables,  $\mathbf{y}_i$ . If individual disciplines are solved separately from each other, the output of discipline  $i$  will not be the same as the coupling variable information input to discipline  $j$ . Therefore, a copy of the discipline  $i$  coupling variables to be used as input to other disciplines must be specified by  $\hat{\mathbf{y}}_i$ . Both the coupling variables and their copies must converge to the same value at an optimal design, so an additional set of consistency constraints in the problem formulation are specified to enforce this condition. These consistency constraints are denoted by  $\mathbf{c}_i^c$  and take the form  $\hat{\mathbf{y}}_i - \mathbf{y}_i = 0$  for each discipline and  $\mathbf{c}$  represents a vector of design constraint functions [51]. The flowchart of AAO algorithm is drawn in Fig. 2, where  $\bar{\mathbf{y}}_i$  is the vector of state variables (variables used inside only one discipline analysis), subscripts  $^*$  represent functions or variables at their optimal value. In AAO, the coupled parameters are also involved in the optimization process. The optimal value is extracted if all disciplines satisfy all the constraints. Otherwise, the design variables are changed and the disciplines are reevaluated [52,53].

In the following, further explanations is provided about the optimization algorithms used in this research.

### 3. MDO problem formulation

Fig. 3 depicts the MDO problem in AAO structure, for the design of a dual-spin vehicle, along with its associated disciplines. As shown, the disciplines employed include structure, aerodynamics, guidance, and control. The aerodynamic discipline aims to maximize the ratio of angle of attack to elevator deflection in trim conditions ( $1/(\alpha/\delta)_{\text{trim}}$ ). The objective of the structure discipline is to minimize the total mass ( $m_t$ ), while the guidance and control discipline seeks to minimize the miss distance ( $md$ ) and control effort ( $ce$ ). Hence, the total objective function ( $J$ ) of the MDO problem with discipline weighting factors ( $k_1, k_2, k_3, k_4$ ) can be formulated as follows

$$J = \min \left( \frac{k_1}{(\alpha/\delta)_{\text{trim}}} + k_2 m_t + k_3 md + k_4 ce \right) \quad (2)$$

In addition to the four terms of the objective function,  $J$ , a substantial penalty value is also added to  $J$  in the event of constraint violations. The MDO problem has totally 15 design variable: 11

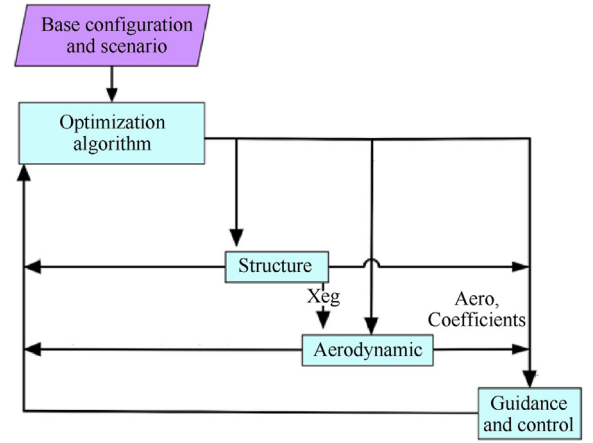


Fig. 3. AAO architecture for dual-spin vehicle configuration design.

variables for internal part of the body, introduced in Tables 1 and 4 design variables for external body elements that introduces in Table 2.

#### 3.1. Structure discipline

In this discipline, all subsystems, including main body, actuator rack, GPS antenna rack, safety and arming rack, dimension of the explosive fuze booster, control and navigation box, roller bearing of the fuze casing, and surrounding casing thicknesses, are considered. By developing a parametric strategy, the projectile mass and moments of inertia can be calculated for each arrangement of components.

As shown in Table 1, the structure discipline design vector consists of 11 elements. The optimal value of these elements will be found after that MDO problem is solved. The maximum allowable acceleration on the projectile and the maximum yield stress of the steel alloy are two constraints in structure discipline. The external diameter of projectile is fixed, but the internal geometry will be optimized to maximize the internal volume. Maximizing the internal volume will minimize the structure mass.

In structural discipline, the mass and moments of inertia of each component, as well as the total projectile mass properties, are calculated parametrically. The amount of stress on each section and the critical stress is also determined. If the stress caused by firing acceleration exceeds the yield stress in each section, a penalty

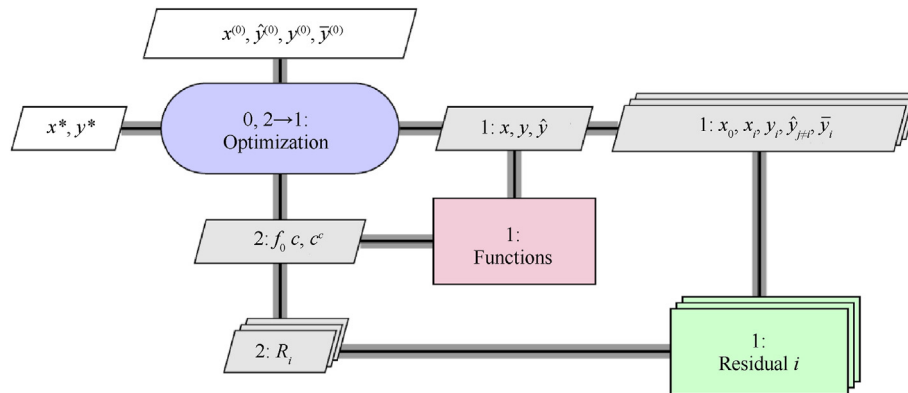
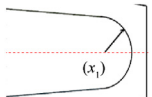
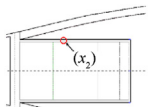
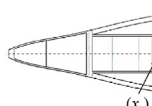
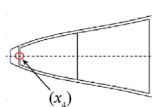
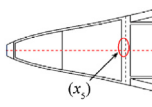
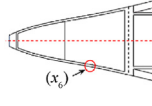
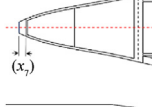
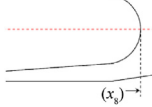
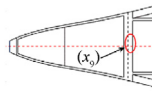
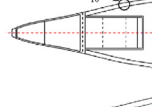
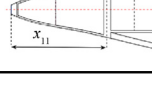


Fig. 2. Flowchart of the AAO algorithm [53].

**Table 1**  
Structure discipline design variables.

Elements		
$x_1$	Internal projectile explosive cylinder radius	
$x_2$	Fuze sequence shell thickness	
$x_3$	Fuze sequence bottom thickness	
$x_4$	Fuze shell nose thickness	
$x_5$	Fuze bottom thickness	
$x_6$	Fuze shell thickness	
$x_7$	Piezoelectric sensor length	
$x_8$	Shell bottom thickness	
$x_9$	Roller-Bearing thickness	
$x_{10}$	Ogive nose shell thickness	
$x_{11}$	Fuze length	

function is added to the objective function. Due to the firing acceleration in the launch tube, the vehicle body undergoes axial and rotational stresses. According to Ref. [54], the highest stress is observed in the axial direction. Therefore, axial stress is taken into consideration as a constraint for the body shell design.

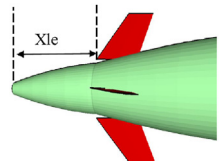
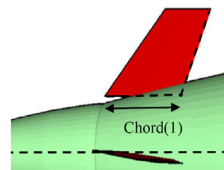
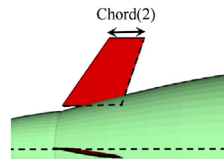
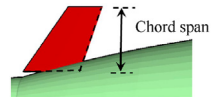
### 3.1.1. Calculation of the mass, center of mass and moment of inertia

Fig. 4(a) shows a solid narrow rectangle of height  $f(x)$  and width  $dx$  that creates a thin disk with thickness  $dx$  around the  $x$ -axis. Fig. 4(b) shows the solid obtained by revolving the functions  $f_1(x)$  and  $f_2(x)$  around  $x$ -axis.

Considering Fig. 4, the mass, center of mass, and moments of inertia of each component can be calculated as follows [55].

$$m = \pi \rho \int_{x_0}^{x_f} (f_2^2(x) - f_1^2(x)) dx \quad (3)$$

**Table 2**  
Aerodynamic discipline design variables.

Elements		
$x_{12}$	distance of the canard leading edge from projectile nose	
$x_{13}$	canard root chord	
$x_{14}$	canard tip root	
$x_{15}$	canard chord span	

**Table 3**  
The relation between longitudinal and directional aerodynamic coefficients [8].

Coefficients	
$C_{m\alpha} = C_{n\beta}$	$C_{mp\beta}^a = C_{np\alpha}^a$
$C_{mq} = C_{nr}$	$C_{m\alpha} = C_{n\beta}$
$C_{m\dot{\alpha}} = C_{n\dot{\beta}}$	$C_{N\dot{\alpha}_e} = C_{Y\dot{\alpha}_e}$
$C_{Yp\alpha}^a = C_{Np\beta}^a$	$C_{m\dot{\alpha}_e} = C_{n\dot{\alpha}_e}$
$C_{Yp\alpha}^f = C_{Np\beta}^f$	$C_{N\alpha} = C_{Y\beta}$
$C_{mp\beta}^f =$	
$C_{np\alpha}^f$	

**Table 4**  
Vehicle initial condition for closed loop and open loop scenarios.

	Closed loop scenario	Open loop scenario
$u_0/(\text{m} \cdot \text{s}^{-1})$	323.16	700
$v_0/(\text{m} \cdot \text{s}^{-1})$	−1.09	0
$w_0/(\text{m} \cdot \text{s}^{-1})$	2.37	0
$\phi_0/(\text{°})$	0	0
$\theta_0/(\text{°})$	−59.16	45
$\psi_0/(\text{°})$	0	0
$p_{a0}/(\text{rad} \cdot \text{s}^{-1})$	880	1418.8
$p_{r0}/(\text{rad} \cdot \text{s}^{-1})$	100	1418.8
$q_0/(\text{rad} \cdot \text{s}^{-1})$	−0.0075	−0.35
$r_0/(\text{rad} \cdot \text{s}^{-1})$	0	0
$x_{m0}/\text{m}$	13817	0
$y_{m0}/\text{m}$	481	0
$h_{m0}/\text{m}$	8202.3	1000

$$X_{Cg} = \frac{\int_{x_0}^{x_f} x (f_2^2(x) - f_1^2(x)) dx}{\int_{x_0}^{x_f} (f_2^2(x) - f_1^2(x)) dx} \quad (4)$$

$$I_x = \frac{\pi \rho}{2} \int_{x_0}^{x_f} (f_2^4(x) - f_1^4(x)) dx \quad (5)$$

$$I_y = \frac{I_x}{2} + \pi \rho \int_{x_0}^{x_f} x^2 (f_2^2(x) - f_1^2(x)) dx \quad (6)$$

where,  $\rho$  is density, and the total mass, center of mass, and moments of inertia of n subsystems can be calculated as follows

$$X_{Cg_t} = \frac{m_1 X_{Cg_1} + m_2 X_{Cg_2} + \dots + m_n X_{Cg_n}}{m_1 + m_2 + \dots + m_n} \quad (7)$$

$$m_t = m_1 + m_2 + \dots + m_n \quad (8)$$

$$I_{xt} = I_{x1} + I_{x2} + \dots + I_{xn} \quad (9)$$

$$I_{yt} = I_{y1} + I_{y2} + \dots + I_{yn} + (X_{Cg_t} - X_{Cg_1})^2 m_1 + \dots + (X_{Cg_t} - X_{Cg_i})^2 m_i + \dots + (X_{Cg_t} - X_{Cg_n})^2 m_n \quad (10)$$

here,  $X_{Cg_t}$  is the center of mass. The  $i$  index is used for the  $i^{\text{th}}$  component,  $m_i$  is the  $i^{\text{th}}$  component mass.

### 3.1.2. Calculation of stresses on different components

The setback pressure is the compressive pressure of the front components that is caused by firing at each cross-section [54]. The acceleration created by the setback force is much larger than rotational acceleration. Therefore, in shell design, the stress due to axial forces acting on the body is a critical point (longitudinal stress is greater than radial and hoop stress). The longitudinal stress on each cross section is calculated by developing a parametric

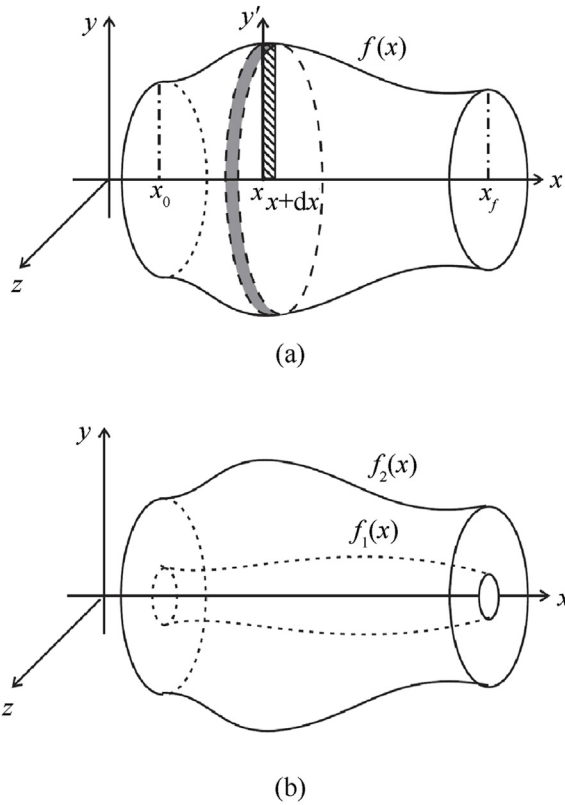


**Fig. 4.** (a)The object obtained from revolving the function  $f(x)$  around the  $x$ -axis; (b) The solid obtained of the revolving of  $f_1(x)$  and  $f_2(x)$  functions around  $x$ -axis [55].

formulation.

As a design constraint, the calculated longitudinal stress must be smaller than the yield stress of each component's material. The maximum yield stress is set to be 1100 MPa. For subsystems such as boards and actuators, depending on the type of hardening used in the fuze, the allowable stress in the design may change from 50 MPa to 180 MPa, which in this research is considered the maximum allowable stress of 120 MPa [56–58]. In order to handle the yield stress constraint, a large penalty value is added to the objective function if the stress constraint is not met.

According to Fig. 5, the compressive force is applied to the bottom and wall of the cylinder. In the thin-walled cylinder, the compressive force is defined by Eq. (11)

$$F = PA = p \frac{\pi D^2}{4} \quad (11)$$

The longitudinal stress in the bottom of a thin-walled section is

equal to the area of this part, which is equal to  $A = \pi Dt$ , where  $D$  is the diameter or caliber and  $t$  is the thickness of the shell. Therefore, the force due to longitudinal stress for a thin-walled closed-end cylindrical vessel is also equal to

$$P_T = \sigma_L \pi Dt \quad (12)$$

In the following, we express the force balance as follows

$$\sum F_H = 0, P_T = F \Rightarrow \sigma_L \pi Dt = p \frac{\pi D^2}{4} \quad (13)$$

If the cylinder has closed ends, then internal pressure can cause a longitudinal stress on the bottom of the thin-walled cylinder that can be obtained from the following equations [54,59].

$$S_1 = \sigma_L = \sigma_{zz} = \frac{pD}{4t} \quad (14)$$

otherwise, the  $S_1 = \sigma_{zz} = 0$ . Internal (or external) pressure always causes hoop stress.

$$S_2 = \sigma_{\theta\theta} = \frac{pD}{2t} \quad (15)$$

In the open-ended cylindrical thick-walled vessels, longitudinal, hoop, and radial stresses are extracted by Eqs. (16)–(18) respectively. Eq. (16) expresses the cross-section longitudinal stress at the cross section, as shown in Fig. 5 as  $S_1$ . The following solutions are known as the Lamé formulas and assume open ends, which implies  $S_1 = 0$  if no axial loads are present. If axial loads are present, they must be accounted for Internal (or external) pressure.

Now, let us look at the axial stress. This is the stress at the point due to two things: the axial inertia of all the materials ahead of the cut setting back and the effective internal pressure caused by the rotation of the projectile and the hydrostatic compression of the fill material [54].

$$S_1 = \sigma_{zz} = \frac{p_i r_i^2 - p_o r_o^2}{(r_o^2 - r_i^2)} - \frac{F_{Axial}}{A} \approx - \frac{F_{Axial}}{\pi (r_o^2 - r_i^2)} \quad (16)$$

We shall use the radii given in the problem statement. We put a negative sign in the aforementioned equation to denote compressive stress because only the axial component loads the inner wall in compression. The force acting on the section of interest due to setback pressure is given by Eq. (16) [54]. Many times, we neglect the first term in the aforementioned equation for conservatism. With this assumption, Eq. (15) can be written as follows: Eq. (17) expresses the amount of hoop stress in thick-walled cylinder geometry shown in Fig. 5 with  $S_2$  [54]. (Note that the subscripts  $o$  and  $i$  refer to the outer and inner surface, respectively.)

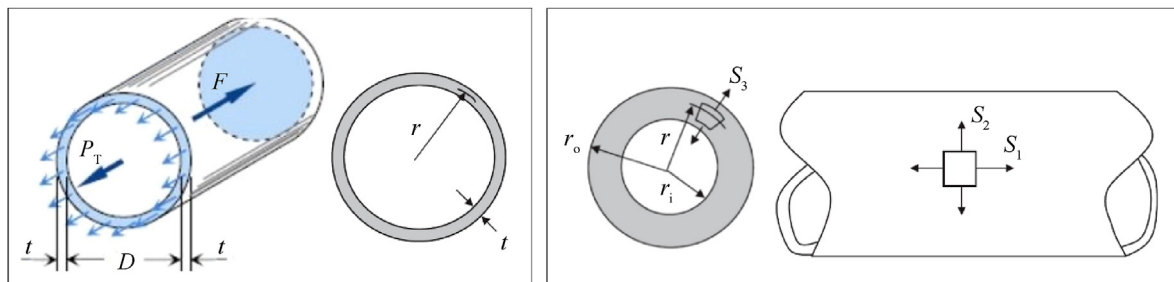


**Fig. 5.** Stress enters in a thin-walled (left) and the thick-walled cylinder (right) [54].



$$S_2 = \sigma_{\theta\theta} = \frac{1}{(r_o^2 - r_i^2)} = \left[ p_i r_i^2 - p_o r_o^2 - \frac{r_i^2 r_o^2 (p_o - p_i)}{r^2} \right] \quad (17)$$

Eq. (18) expresses the amount of radial stress in thick-walled cylinder geometry shown in Fig. 5 with  $S_3$  [54].

$$S_3 = \sigma_{rr} = \frac{1}{(r_o^2 - r_i^2)} = \left[ p_i r_i^2 - p_o r_o^2 + \frac{r_i^2 r_o^2 (p_o - p_i)}{r^2} \right] \quad (18)$$

here,  $r_i$ ,  $r_o$  and  $t$  are internal radial, external radial and thickness of bottom side of thin-walled cylinder respectively.

To calculate the longitudinal stress on the bottom of cylinders in the projectile shell and subsystems, the vehicle shell is assumed to be a thin-walled cylinder. To calculate the longitudinal stress in the wall of the body shell and subsystems, the vehicle is assumed to be a thick-walled cylinder in this paper. The longitudinal stress on the bottom side of the cylinder containing pressure  $p$ , which is generated from launch acceleration from front mass components [59].

### 3.2. Aerodynamic discipline

Similar to the structure discipline, a parametric formulation is developed to account for the effects of geometric configuration changes on aerodynamic characteristics during optimization iterations. Missile-Datcom [60], an engineering software, is used as the base software to calculate the aerodynamic coefficients.

By developing a code in the Matlab software, an input file for Missile-Datcom, namely foor005.dat, is generated in a parametric manner. Hence, by changing the desired geometric characteristics, the aerodynamic model data can be derived. In order to redesigning the outer shape of the projectile, a canard needs to be added and the length of the projectile needs to be changed. To do this, four of the geometric characteristics needed for the Missile-Datcom software are set to be variable, while the others are fixed. These variables form the aerodynamic discipline design vector, which is shown in Table 2.

The objective of aerodynamic discipline is to get maximum aerodynamic control effectiveness, i.e., to minimize the ratio of  $(1/(\alpha/\delta_e)_{\text{trim}})$  in trim conditions. The value of  $\alpha/\delta_e$  can be calculated from the following Equation that says, total moment on vehicle in trim conditions is equal to zero

$$Cm_{\alpha}\alpha + Cm_{\delta_e}\delta_e = 0 \quad (19)$$

which results

$$\frac{\alpha}{\delta_e} = \frac{-Cm_{\delta_e}}{Cm_{\alpha}} \quad (20)$$

### 3.3. Guidance and control discipline

The dynamic model of a dual-spin vehicle can be expressed in seven degrees of freedom. Typically, this model is derived in a Body-Fixed Plane (BFP) frame instead of a conventional rotating body frame. The difference between these frames is that the BFP frame does not rotate in the roll axis, i.e.,  $\dot{\phi}_{F,BFP} = 0$ . Nonlinear 7-DoF equations of motion in the BFP frame are presented here [61]

$$\begin{bmatrix} \dot{u}_B \\ \dot{v}_B \\ \dot{w}_B \end{bmatrix} = \frac{1}{m} \begin{bmatrix} F_x \\ F_y \\ F_z \end{bmatrix} + g \begin{bmatrix} -\sin \theta \\ 0 \\ \cos \theta \end{bmatrix} - \begin{bmatrix} 0 & -r & q \\ r & 0 & r \tan \theta \\ -q & -r \tan \theta & 0 \end{bmatrix} \begin{bmatrix} u_B \\ v_B \\ w_B \end{bmatrix} \quad (21)$$

$$\begin{bmatrix} \dot{p}_f \\ \dot{p}_a \\ \dot{q} \\ \dot{r} \end{bmatrix} = \begin{bmatrix} m_{l,f}/I_x^f \\ m_{l,a}/I_x^a \\ m_m/I_y^T \\ m_n/I_z^T \end{bmatrix} - \begin{bmatrix} 0 \\ 0 \\ \frac{r(p_f I_x^f + p_a I_x^a)}{I_y^T} + r^2 \tan \theta \\ \frac{q(p_f I_{xx}^f + p_a I_{xx}^a)}{I_z^T} - q r \tan \theta \end{bmatrix} \quad (22)$$

$$\begin{bmatrix} \dot{\phi}_f \\ \dot{\phi}_a \\ \dot{\theta} \\ \dot{\psi} \end{bmatrix} = \begin{bmatrix} 1 & 0 & 0 & \tan \theta \\ 0 & 1 & 0 & \tan \theta \\ 0 & 0 & 1 & 0 \\ 0 & 0 & 0 & 1/\cos \theta \end{bmatrix} \begin{bmatrix} p_f \\ p_a \\ q \\ r \end{bmatrix} \quad (23)$$

$$\begin{bmatrix} \dot{x} \\ \dot{y} \\ \dot{z} \end{bmatrix}_E = \begin{bmatrix} \cos \theta \cos \psi & -\sin \psi & \sin \theta \cos \psi \\ \cos \theta \sin \psi & \cos \psi & \sin \theta \sin \psi \\ -\sin \theta & 0 & \cos \theta \end{bmatrix} \begin{bmatrix} u_B \\ v_B \\ w_B \end{bmatrix} \quad (24)$$

Taking into account the axial symmetry property of the plant, aerodynamic longitudinal and directional coefficients are the same in magnitude, as shown in Table 3 [8].

The aerodynamic forces are calculated as follows [2,8,15,61].

$$F_x = \bar{q} S_{\text{ref}} (C_{A_{\text{fore-body}}} + C_{A_{\text{aft-body}}}) \quad (25)$$

$$F_y = \bar{q} S_{\text{ref}} \left( C_{Y_{\beta}} \beta + C_{Y_p} \alpha \frac{p_a D_{\text{ref}}}{2V} + C_{Y_{\delta_y}} \delta_y \right) \quad (26)$$

$$F_z = -\bar{q} S_{\text{ref}} \left( C_{N_{\alpha}} \alpha + C_{N_p} \beta \frac{p_a D_{\text{ref}}}{2V} + C_{N_{\delta_z}} \delta_z \right) \quad (27)$$

The aerodynamic moment are

$$\begin{bmatrix} m_{l,f} \\ m_{l,a} \\ m_m \\ m_n \end{bmatrix} = \bar{q} S_{\text{ref}} D_{\text{ref}} \left( \begin{bmatrix} C_{l_{\delta}} \\ 0 \\ C_{m0} \\ C_{n0} \end{bmatrix} + \left( \frac{D_{\text{ref}}}{2V} \right) \begin{bmatrix} C_{l_p} p_f \\ C_{l_p} p_a \\ C_{m_q} q \\ C_{n_r} r \end{bmatrix} + \left( \frac{p_a D_{\text{ref}}}{2V} \right) \right. \\ \left. \times \begin{bmatrix} 0 \\ 0 \\ C_{m_p} \\ C_{n_p} \end{bmatrix} + \begin{bmatrix} 0 \\ 0 \\ C_{m_{\delta_z}} \delta_z \\ C_{n_{\delta_y}} \delta_y \end{bmatrix} \right) + \begin{bmatrix} m_{f,a} - m_{f,a} \\ 0 \\ 0 \end{bmatrix} \quad (28)$$

where,

$$m_{f,a} = F_x D_{\text{ref}} \text{sign}(p_a - p_f) (k_s + k_v |p_a - p_f|) \quad (29)$$

here,  $k_s$ , and  $k_v$ , are the friction coefficients between the fore body and aft body. To check the controllability constraint, the nonlinear equations of motion are linearized in a parametric manner. In this way, the Jacobian of the nonlinear equations is derived, and after that, the state space form of the equations is derived for three channels, including the longitudinal channel, directional channel,

and lateral channel. The parametric linearized equation of motion in the longitudinal channel is

$$\begin{bmatrix} \dot{w} \\ \dot{q} \\ \dot{\theta} \end{bmatrix} = \mathbf{A}_{\text{long}} \begin{bmatrix} w \\ q \\ \theta \end{bmatrix} + \mathbf{B}_{\text{long}} \delta_e \quad (30)$$

where,

$$\begin{bmatrix} \dot{p}_f \\ \dot{\phi}_f \end{bmatrix} = \mathbf{A}_{\text{lat}} \begin{bmatrix} p_f \\ \phi_f \end{bmatrix} + \mathbf{B}_{\text{lat}} \delta_A \quad (32)$$

where,

$$\mathbf{A}_{\text{lat}} = \begin{bmatrix} t_1 + t_2 + t_3 & 0 \\ 1 & 0 \end{bmatrix}$$

$$\mathbf{A}_{\text{long}} = \begin{bmatrix} -\frac{1}{2} \rho V^2 S_{\text{ref}} D_{\text{ref}} \left( \frac{CN_{\alpha}}{V} + (CN_{p\alpha} D_{\text{ref}} p_a) / (2V^2) \right) / m_t & u & rv(\tan^2 \theta + 1) \\ \frac{1}{2} \rho V S_{\text{ref}} D_{\text{ref}} C m_{\alpha} / I_y^T & \frac{1}{4} \rho S_{\text{ref}} D_{\text{ref}}^2 V C m_q / I_y^T & -r^2 (\tan^2 \theta + 1) \\ 0 & 1 & 0 \end{bmatrix}$$

and

$$\mathbf{B}_{\text{long}} = \begin{bmatrix} \frac{1}{2} \rho V^2 S_{\text{ref}} D_{\text{ref}} CN \delta_e / m_t \\ \frac{1}{2} \rho V^2 S_{\text{ref}} D_{\text{ref}} C m_{\delta_e} / I_y^T \\ 0 \end{bmatrix}$$

Parametric linearized equations in directional channel are derived as

$$\begin{bmatrix} \dot{v} \\ \dot{r} \\ \dot{\psi} \end{bmatrix} = \mathbf{A}_{\text{dir}} \begin{bmatrix} v \\ r \\ \psi \end{bmatrix} + \mathbf{B}_{\text{dir}} \delta_R \quad (31)$$

where,

and

$$\mathbf{B}_{\text{lat}} = \begin{bmatrix} \frac{1}{2} \rho V S_{\text{ref}} D_{\text{ref}} C l_{\delta a} / I_x^f \\ 0 \end{bmatrix}$$

$$t_1 = \frac{1}{4} \rho S_{\text{ref}} D_{\text{ref}}^2 V C l_p / I_x^f$$

$$t_2 = -\rho V^2 S_{\text{ref}} D_{\text{ref}} C A_f \text{dirac}(p_a - p_f) (K_s - K_v |p_a - p_f|) / I_x^f$$

$$t_3 = -\frac{1}{2} \rho V^2 S_{\text{ref}} D_{\text{ref}} C A_f K_v \text{sign}(p_a - p_f)^2 / (I_x^f)$$

In a linear time-invariant system, controllability is checked by calculating the rank of the following matrix

$$\mathbf{A}_{\text{dir}} = \begin{bmatrix} \frac{1}{2} \rho V^2 S_{\text{ref}} D_{\text{ref}} \left( \frac{CY_{\beta}}{V} + (CN_{p\alpha} D_{\text{ref}} p_a) / (2V^2) \right) / m_t & -u - w \sin \theta & 0 \\ \frac{1}{2} \rho V S_{\text{ref}} D_{\text{ref}} C n_{\beta} / I_y^T & q \tan(\theta) - \frac{1}{4} \rho S_{\text{ref}} D_{\text{ref}}^2 V C n_r / I_y^T & 0 \\ 0 & 1 / \cos \theta & 0 \end{bmatrix}$$

and

$$\mathbf{B}_{\text{dir}} = \begin{bmatrix} \frac{1}{2} \rho V^2 S_{\text{ref}} D_{\text{ref}} C Y_{\delta_r} / m_t \\ \frac{1}{2} \rho V^2 S_{\text{ref}} D_{\text{ref}} C n_{\delta_r} / I_y^T \\ 0 \end{bmatrix}$$

State space form in lateral channel is

$$\zeta = [\mathbf{B}, \mathbf{A}\mathbf{B}, \mathbf{A}^2\mathbf{B}, \dots, \mathbf{A}^{k-1}\mathbf{B}]$$

If the  $\zeta$  matrix is full rank, the system is called controllable for all control channels (longitudinal, directional, and lateral). After conducting various simulations, it was observed that controllability at the beginning of guidance is more critical. Therefore, this point is considered as controllability constraint checkpoint. The MDO problem is structured such that if the controllability constraint is not met in the guidance and control discipline, a large penalty value



will be added to the objective function. Another constraint in the guidance and control discipline is the gyroscopic stability constraint. The gyroscopic and dynamic stability factors can be expressed as shown [10].

$$S_G = \frac{I_x^T \tilde{p}}{2I_y^T M} \quad (33)$$

$$S_D = \frac{2(CN_\alpha - C_{x0}) + G^T p^*}{(CN_\alpha - 2C_{x0}) - \left(\frac{mD^2}{I_y^T}\right)(Cm_q)/2} \quad (34)$$

where

$$\tilde{p} = \frac{p_f + \gamma_{DS} p_a}{1 + \gamma_{DS}} \quad (35)$$

$$\gamma_{DS} = I_x^a / I_x^f \quad (36)$$

$$I_x^T = I_x^f + I_x^a = I_x^f (1 + \gamma_{DS}) \quad (37)$$

$$M = \rho S V^2 C m_\alpha \quad (38)$$

$$p^* = \frac{(p_f + \mu_{DS} p_a)}{(1 + \mu_{DS})} \quad (39)$$

$$\mu_{DS} = \frac{(Rm_{ax} + r_{ax})C_{NP\alpha}^a}{(Rm_{fx} + r_{fx})C_{NP\alpha}^f} \quad (40)$$

The inertia-weighted average spin rate  $\tilde{p}$  is biased towards the spin rate of the body with the largest roll inertia component. The Magnus-weighted average spin rate  $p^*$  behaves in precisely the same manner as  $\tilde{p}$ ; however, it is biased towards the body with the largest Magnus moment. The inertia ratio is  $\gamma_{DS}$ , and the Magnus ratio is  $\mu_{DS}$ .  $r_{fx}$  and  $r_{ax}$  are the fixed plane components of the vector from the composite center of mass to the forward and aft body mass centers, respectively.  $Rm_{fx}$  is the fixed-plane component of the vector from the forward body mass center to the forward body Magnus center pressure, and  $Rm_{ax}$  is the fixed-plane component of

the vector from the aft-body mass center to the aft-body Magnus center pressure. The gyroscopic stability is met when  $S_G > 1$ . The criteria for dynamic stability in spin-stabilized vehicles is to have  $0 < S_D < 2$  [4].

### 3.3.1. Closed loop system design

A cascaded three-loop controller is designed to control the dual-spin vehicle. The inner loop controls angular rates  $p$ ,  $q$  and  $r$ . The intermediate loop controls angle of attack, sideslip angle and fore body roll angle. The outer loop controls lateral accelerations. A PI-based dynamic inversion controller is used for designing inner loop and second loop. Moreover, an adaptive PID model based controller is designed for outer loop design. The performance of this control system is evaluated, previously by authors in Ref. [62]. Fig. 6 shows the schematic of the control systems used in optimization loop.

According to a predefined flight scenario, the vehicle travels along its ballistic path until it reaches the peak of the trajectory. At this point, guidance and control are activated, and it will continue along a guided trajectory towards the target. The guidance system is designed based on proportional navigation with compensation for the effect of gravity. The acceleration commands in body coordinates are given by [6].

$$[a]^B = N [\omega^{OE}]^B \times [v_{TB}^E]^B - \frac{1}{|g|} [T]^{BE} [g]^L \quad (41)$$

here,  $N$  is the proportional navigation coefficient.  $s_{TB}$  is the vehicle-target relative distance vector.  $[v_{TB}^E]^E$  is the relative velocity vector between the vehicle and target in the inertial coordinate system.  $[T]^{BE}$  is the transformation matrix from the inertial to body coordinate system. The variable  $[\omega^{OE}]^B$  is the rate of line of sight (LOS) with respect to the inertial frame, projected in the body coordinate system, and can be calculated as

$$[\omega^{OE}]^B = \frac{[T]^{BE} [s_{TB}]^E \times [v_{TB}^E]^E}{|s_{TB}|^2} \quad (42)$$

When the vehicle approaches the target, a saturation limit is used for acceleration due to the decreasing value of  $|s_{TB}|^2$ . Finally,  $[g]^L = [0, 0, g]^T$  represents the gravity vector in the inertial coordinate system.

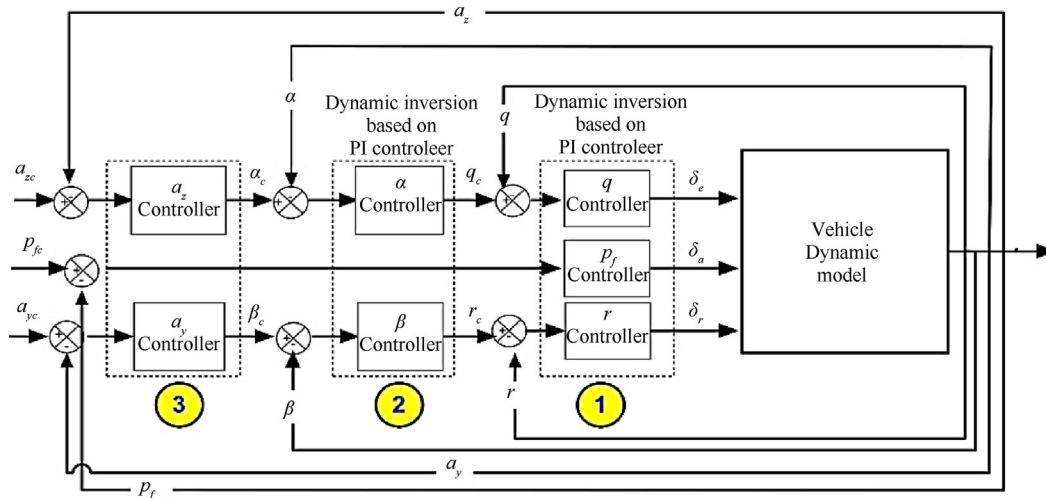


Fig. 6. Autopilot structure used in the 7.degree simulation in the optimization algorithm [62].

The objective of the guidance and control discipline is to minimize the miss distance between the vehicle and the target and Control Effort ( $ce$ ) which can be calculated as follows

$$md = \min \left( \sqrt{(x_m - x_t)^2 + (y_m - y_t)^2 + (h_m - h_t)^2} \right) \quad (43)$$

$ce$  is defined as the sum of absolute values of deflection angles of equivalent control surfaces

$$ce = \sum_{i=1}^n (|\delta_a(i)| + |\delta_e(i)| + |\delta_r(i)|) \quad (44)$$

where,  $n$  is number of time steps in simulation  $x_m, y_m$ , and  $h_m$  represent the vehicle's position, and  $x_t, y_t$ , and  $h_t$  are the three components of the target position vector [63]. Controllability and gyroscopic stability constraints are checked in each iteration of the optimization process, and a large penalty value will be added to the objective function if any of these constraints are not met.

### 3.4. Optimization algorithms

For solving the formulated the MDO problem, two search algorithms are utilized and the resulting optimal configurations are compared. The first is a classic optimization approach, namely Minimax and the second is a heuristic optimization approach called Simulated Annealing (SA). Minimax approach, minimizes the worst-case (largest) value of a set of multivariable functions, starting at an initial estimate

$$\min_x \max_i (f_i(x)) \text{ such that } \begin{cases} c(x) < 0 \\ c_{eq}(x) = 0 \\ Ax \leq b \\ A_{eq}x = b_{eq} \\ l_b \leq x \leq u_b \end{cases} \quad (45)$$

where,  $c(x)$ ,  $c_{eq}(x)$  and  $f(x)$  are functions of non-equality constraints, equality constraints and objective function, respectively. The minimax problem will be reformulates into an equivalent Nonlinear Linear Programming problem by appending additional (reformulation) constraints of the form  $f_i(x) \leq \gamma$  to the constraints given in Eq. (45), and then minimizing  $\gamma$  over  $x$ . A sequential quadratic programming (SQP) method is used to solve this problem [64].

Simulated Annealing is a probabilistic metaheuristic algorithm inspired by the annealing process in metallurgy. This algorithm is commonly used to solve optimization problems by searching for the global optimum in a large solution space. The main idea behind simulated annealing is to mimic the annealing process of slowly cooling a material to reduce its defects and increase its stability. The algorithm starts with an initial solution and iteratively explores

neighboring solutions by making small modifications. It evaluates the quality of each solution using an objective function and accepts better solutions unconditionally. However, it also accepts worse solutions with a certain probability determined by a cooling schedule. The cooling schedule controls the exploration-exploitation trade-off by gradually reducing the probability of accepting worse solutions as the algorithm progresses. Initially, the algorithm is more likely to accept worse solutions to explore a wider solution space. As the temperature decreases, the acceptance probability decreases, leading the algorithm to converge towards the global optimum. Simulated Annealing is effective in escaping local optima and finding near-optimal solutions in complex optimization problems. It provides a good balance between exploration and exploitation, enabling the algorithm to explore different regions of the solution space while converging towards the best solution [65].

## 4. Results and discussion

The proposed algorithms are implemented in two scenarios, including open loop and closed loop simulations. The vehicle's initial conditions are shown in Table 4. For the closed loop scenario, a fixed target is considered at  $[x_t, y_t, h_t] = [17800, 480, 1000]$  (m).

The proposed MDO problem is solved by the minimax and SA algorithms. The upper and lower bounds of all 15 optimization design variables, as well as the optimal values calculated by the SA and minimax algorithms, are shown in Table 5. Additionally, the base design vector, which is an initial guess for the design variables within the feasible region, is also included in Table 5. The resulting optimal and base configurations, along with the upper and lower bounds for the design variables, are presented in Fig. 7.

The resulting values for different objectives are shown in Table 6. According to Table 6, the SA algorithm provides the lowest value for the objective function ( $J$ ) of Eq. (2). SA proposes a configuration that has the smallest mass and control effort for the projectile. The Minimax algorithm gives a better value for the elevator to angle of attack ratio. All three configurations satisfy yield stress, controllability, miss distance lower than 1 m constraints, and gyroscopic stability. For controllability constraint evaluation, the controllability matrices  $\zeta$  for the base, SA, and minimax configurations in each channel are extracted. For example, in the case of SA algorithm, controllability matrices  $\zeta$  for longitudinal, directional and lateral channels is as follows

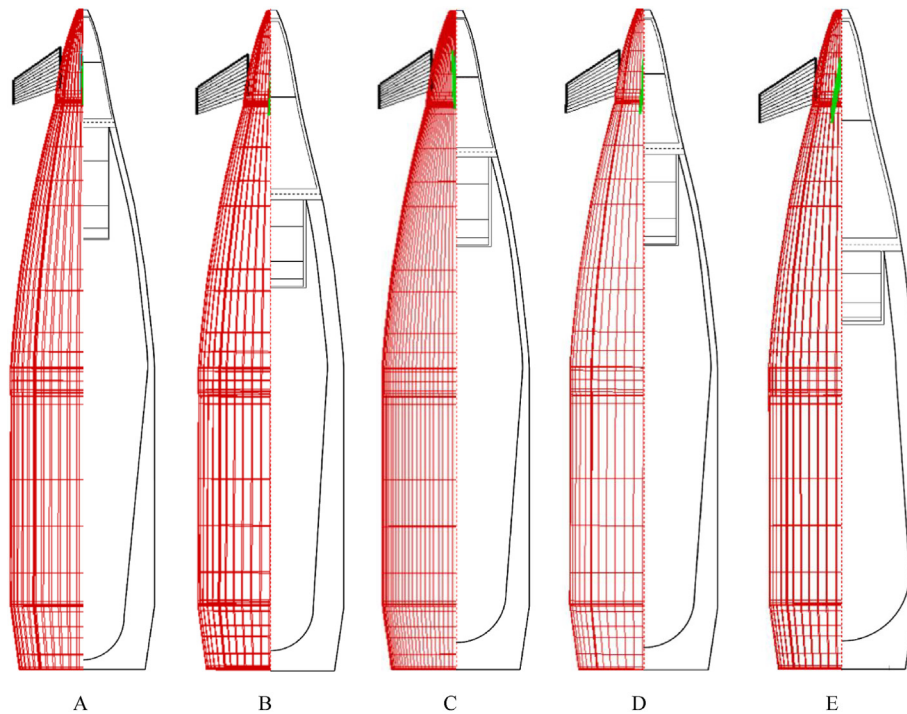
$$\zeta_{\text{lon-SA}} = \begin{bmatrix} 3.27 & 88623.63 & -51476.75 \\ 274.24 & -153.81 & 152316.31 \\ 0 & 274.24 & -153.81 \end{bmatrix}$$

$$\zeta_{\text{lat-SA}} = \begin{bmatrix} 44792.31 & -1575304.28 & 0 & -1962063377.98 \\ 0 & 7744.29 & -273698.680 & 9659373.02 \\ 0 & 44792.31 & -1575304.28 & 55595247.60 \\ 0 & 0 & 7744.29 & -273698.68 \end{bmatrix}$$

**Table 5**

Optimum values of design variables in comparison with that of upper and lower bounds and the base values.

MDO design variables listed in Table 1	Lower bound/m	Base value of design variables/m	Minimax results/m	SA results/m	Upper bound/m
$x_1$	0.045	0.04500	0.052539063	0.052766272	0.0720
$x_2$	0.001	0.00299	0.002492188	0.002637732	0.0030
$x_3$	0.001	0.00140	0.001795313	0.001426017	0.0030
$x_4$	0.001	0.00310	0.001495313	0.001926211	0.0035
$x_5$	0.004	0.00539	0.004495313	0.005746507	0.0070
$x_6$	0.002	0.003138	0.002492202	0.003381752	0.0040
$x_7$	0.007	0.0086645	0.007523438	0.008577225	0.0090
$x_8$	0.010	0.021680	0.029037356	0.023968513	0.0300
$x_9$	0.005	0.006155	0.005507813	0.006531367	0.0070
$x_{10}$	0.007	0.017278	0.007000000	0.007000091	0.0200
$x_{11}$	0.120	0.195160	0.150468750	0.147444045	0.2500
$x_{12}$	0.040	0.046200	0.041000000	0.044031735	0.0500
$x_{13}$	0.043	0.045132	0.043100000	0.047466186	0.0480
$x_{14}$	0.026	0.028840	0.026000000	0.030891301	0.0310
$x_{15}$	0.050	0.054220	0.055000000	0.056134962	0.0600

**Fig. 7.** The Optimal configuration results: (A) Configuration with lower bound values; (B) Base configuration; (C) Optimum configuration obtained by Minimax; (D) Optimum configuration obtained by SA; (E) Configuration with upper bound values.**Table 6**

Projectile MDO results comparison.

	$J$	$m_t$	$m_{\text{forward}}$	$(\delta/\alpha)_{\text{trim}}$	Control Effort	Yield Stress	Controllability	$MD < 1 \text{ m}$	$S_G$ at $MV = 700$	$S_D$ at $MV = 700$
Base	90.0724953	46.76484	2.53993	0.471749	197.2016	Passed	Passed	Passed	3.7	0.595
SA	77.2398744	37.53757	1.39961	0.497853	148.0963	Passed	Passed	Passed	2.24	0.66
Minimax	77.9958155	37.81333	1.33456	0.467784	167.9326	Passed	Passed	Passed	2.31	0.67

$$\zeta_{\text{dir-SA}} = \begin{bmatrix} 3.27 & -88065.71 & -48749.92 \\ 274.24 & 0.00157.34 & 1.51205.670 \\ 0 & 534.95 & 306.92 \end{bmatrix}$$

All these three matrices are full rank.

#### 4.1. Evaluation of yield stress constraint

To demonstrate the satisfaction of the yield stress constraint, various sections on the surfaces and walls of the projectile are labeled in Fig. 8. As can be seen in Fig. 8, the lower bound configuration yield stress is higher than maximum allowable yield stress. It must be noted that lower bound and upper bound configurations may not necessarily meet the constraints and may fall outside the

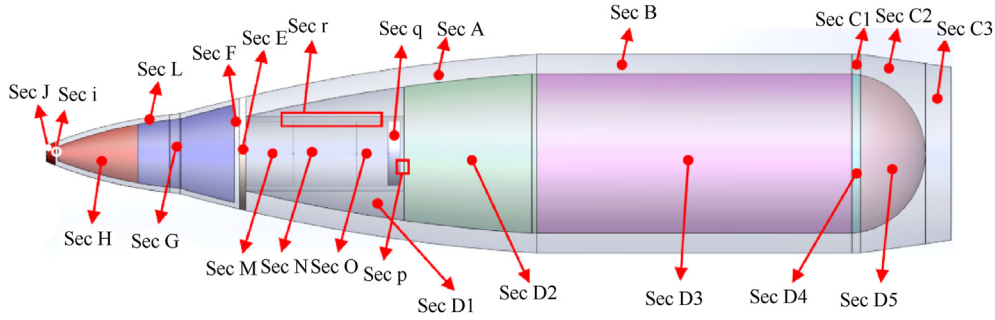


Fig. 8. Labeling different section on vehicle body.

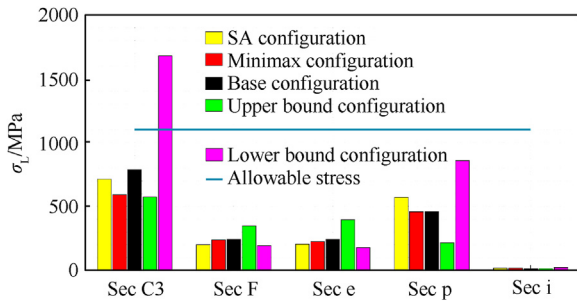


Fig. 9. Bar chart of stress in bottom of components on optimal, base, lower and upper bound configurations.

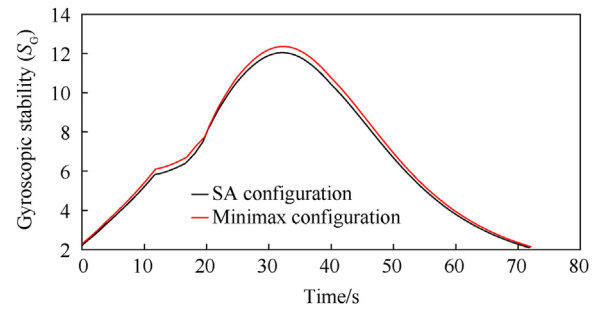


Fig. 11. Evaluation of gyroscopic stability for minimax and SA configurations.

feasibility region. However, all optimal configurations have met the yield stress constraint.

The maximum values of longitudinal stresses (at the bottom of sections and the wall sections) in different sections for SA, minimax, base, lower, and upper bound configurations are depicted in Figs. 9 and 10. It is evident that the optimum configurations experience stresses that are lower than the yield stress, thereby satisfying the yield stress constraint.

#### 4.2. Stability constraints evaluation

Here, an open-loop simulation is performed, considering the initial conditions of Table 4, and stability criteria are evaluated throughout the entire flight trajectory, from vehicle launch up to reaching the ground. Variations of gyroscopic and dynamic stability parameters,  $S_G$  and  $S_D$ , with time are depicted in Fig. 11, and Fig. 12

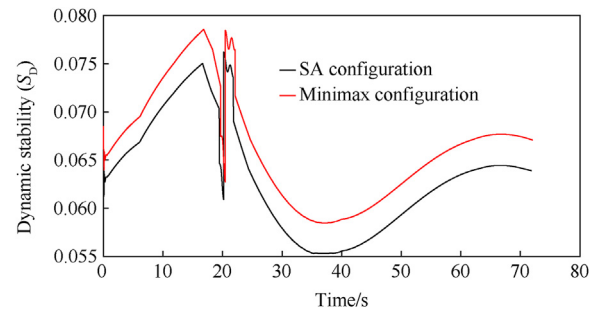


Fig. 12. Comparison the dynamic stability of minimax, and SA configurations.

for the optimum configurations obtained from SA and minimax. As previously mentioned, gyroscopic and dynamic stability are achieved when  $S_G > 1$  and  $0 < S_D < 2$ . It can be observed that the

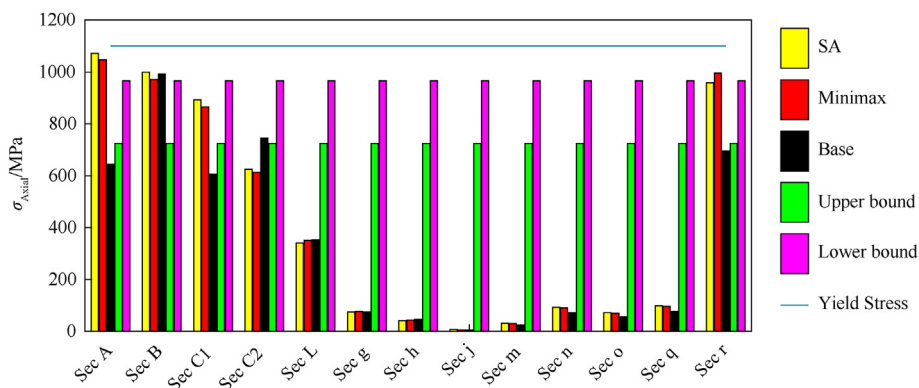


Fig. 10. Bar chart of the axial stresses on component of cylindrical walls on optimal, base, lower and upper bound configurations.

resulting configurations maintain gyroscopic and dynamic stability throughout the full flight trajectory.

#### 4.3. Control effort criteria and object function behavior evaluation

Another parameter included in the objective function is the control effort, which is defined in Eq. (3). Fig. 13 shows the amount of control effort along the guided scenario for two optimal configurations obtained from the SA and minimax solvers. As can be seen, the SA solver has a lower amount of control effort than the minimax solver.

The optimization objective function ( $J$ ) for both SA and minimax algorithms is drawn in Figs. 14 and 15. The final optimum values are also shown. As can be seen, SA gives a lower value for the objective function, and hence it has a better convergence behavior.

#### 4.4. Vehicle behavior during guided phase

Utilizing the initial conditions of a closed-loop scenario, according to Table 4, the time histories of some state variables are drawn. Figs. 16 and 17 present variations in the lateral accelerations  $a_y$  and  $a_z$  of the vehicle for three configurations, namely SA,

minimax, and base. As shown, SA shows a faster and smoother trend.

Aft-body and fore-body roll rates during the guided trajectory are shown in Figs. 18 and 19. The aft-body has a high roll rate but with a decreasing trend due to the roll damping coefficient ( $C_{lpa}$ ). Regarding the fore-body, the designed control system ensures that the fore-body roll rate reaches zero within a settling time of less than 0.2 s.

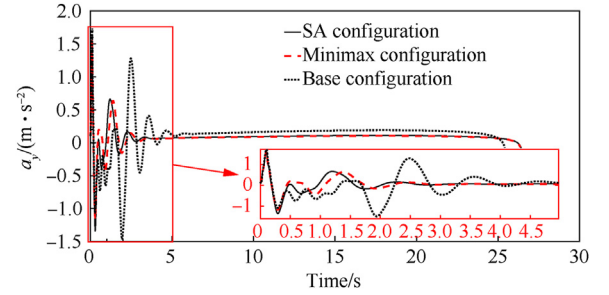


Fig. 16. Time history of  $a_y$  for base, minimax and SA configurations.

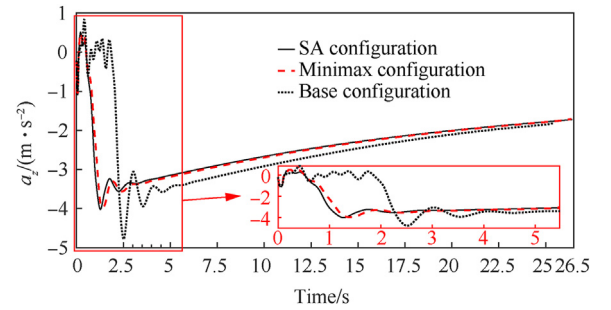


Fig. 17. Time history of  $a_z$  for base, minimax and SA configurations.

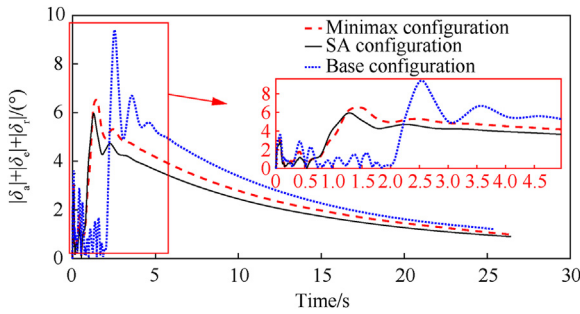


Fig. 13. Variation of control effort during the guided phase.

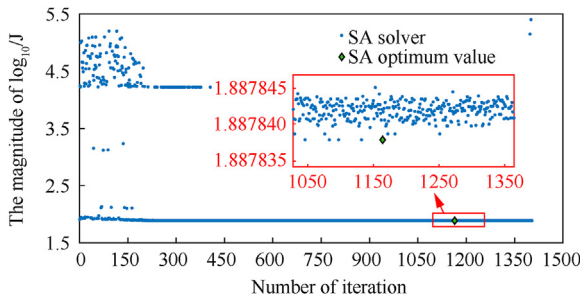


Fig. 14. SA algorithm convergence behavior during optimization iterations.

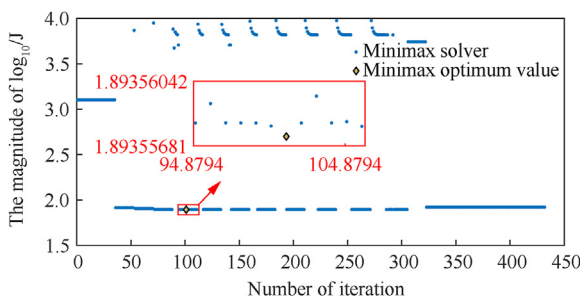


Fig. 15. Minimax algorithm convergence behavior during optimization iterations.

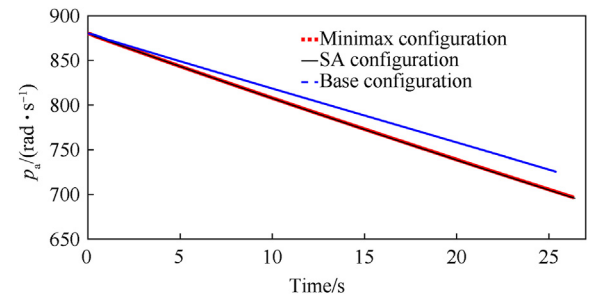


Fig. 18. Time history of aft body roll rate for base, minimax and SA configurations in guidance phase.

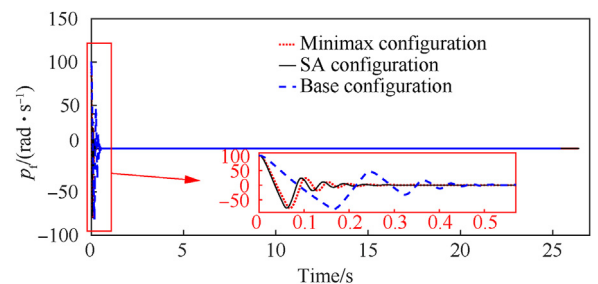


Fig. 19. Time history of forward roll rate for base, minimax and SA configurations.



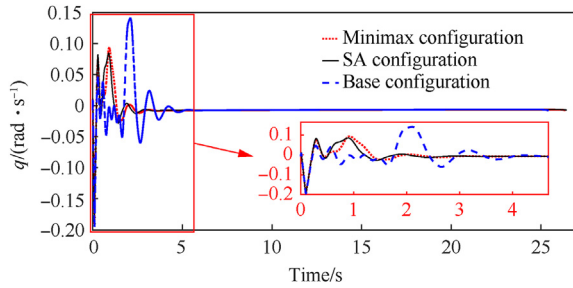


Fig. 20. Time history of pitch rate for base, minimax and SA configurations.

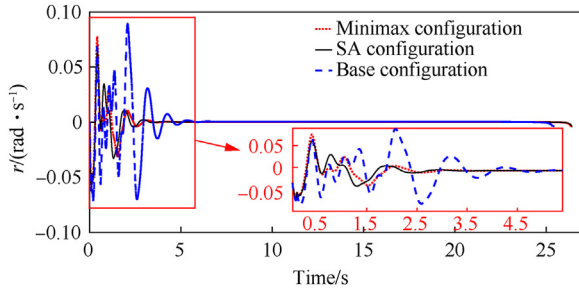


Fig. 21. Time history of yaw rate for base, minimax and SA configurations.

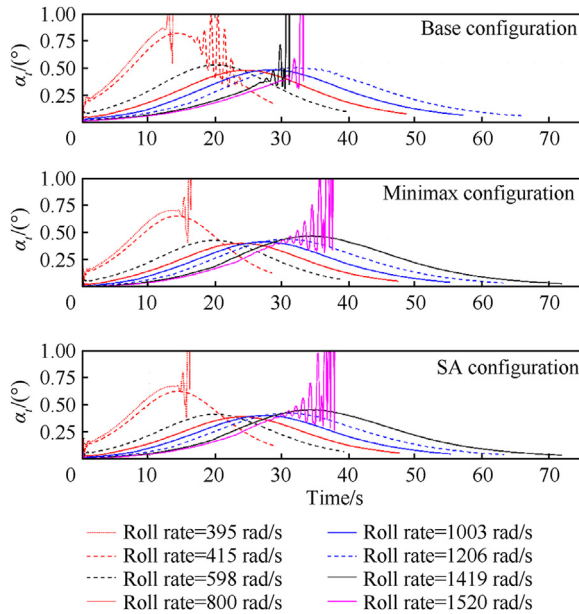


Fig. 22. Angle of Incidence  $\alpha_t$  in different roll rate values for base, Minimax and SA configurations.

Table 7

Critical roll rate values.

	Minimum critical roll rate, $\text{rad} \cdot \text{s}^{-1}$ (corresponding muzzle velocity, $\text{m} \cdot \text{s}^{-1}$ )	Maximum critical roll rate, $\text{rad} \cdot \text{s}^{-1}$ (corresponding muzzle velocity, $\text{m} \cdot \text{s}^{-1}$ )
Base configuration	598 (295)	1206 (595)
SA	415 (205)	1419 (700)
Minimax	415 (205)	1419 (700)

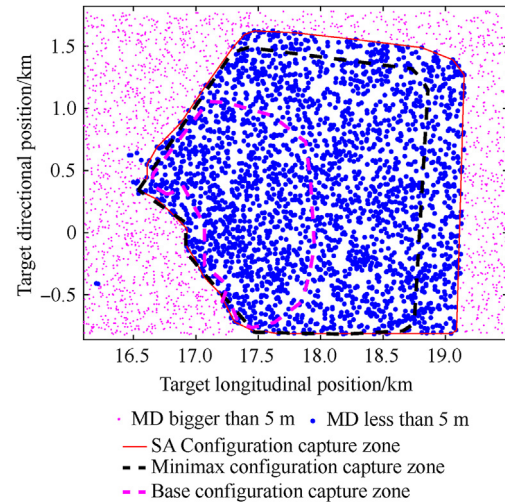


Fig. 23. Capture zone base, Minimax and SA configurations.

Vehicle pitch and yaw rates are shown in Figs. 20 and 21. SA and minimax configurations have a similar manner in pitch and yaw rates.

As shown, all three configurations have a satisfactory behavior in closed loop simulation and all states are within the acceptable range during closed loop flight.

#### 4.5. Critical roll rates assessment

The objective of this section is to calculate the critical initial roll rates for the configurations at hand. In this way, an open-loop simulation is conducted with different initial roll rates. On the other hand, the initial roll rate  $p_0$  can be determined by Ref. [66].

$$p_0 = 2\pi V_0 / (nD) \quad (46)$$

where  $V_0$  is the muzzle velocity,  $D$  is the caliber, and  $n$  is a constant value called rifling twist, with  $n = 20$ . The total angle of attack,  $\alpha_t = \sqrt{\alpha^2 + \beta^2}$  versus time for different initial roll rates is shown in Fig. 22. The summarized results for the minimum and maximum allowable roll rates, i.e., the critical roll rates, are shown in Table 7. The SA and minimax configurations have similar values for critical roll rates and a higher range for allowable roll rates compared to that of the base configuration.

According to the relationship  $p_0 = 2\pi V_0 / (nD)$ , the amount of spin rate of a projectile is proportional to the muzzle velocity. The more unstable the projectile configuration is, the higher spin rate is required for gyroscopic stability. For this reason, the base configuration requires a higher Muzzle velocity compared to optimal configurations.



**Table 8**  
Capture zone characteristics of three configurations.

	Number of runs	Number of MD <5 m	Capture zone area/km <sup>2</sup>
Base Configuration	5000	1055	1.499
SA Configuration	5000	2960	5.067
Minimax Configuration	5000	2404	4.052

#### 4.6. Capture zone calculation

Here, the capture zone of three configurations is calculated via 5000 successive runs of the closed loop scenario. In this way, the vehicle's initial conditions are set according to Table 4, and the target position is changed in each run with a uniformly distributed random manner, modeled as follows

$$[x_t, y_t, h_t]^T = [17800, 480, 1000]^T \pm [1700\text{rand}(0, 1), 1300\text{rand}(0, 1), 0]^T \quad (48)$$

As shown in Fig. 23, blue points represent locations with miss distances less than 5 m, while red points indicate locations with miss distances greater than 5 m.

The SA configuration has the largest capture zone compared to the minimax and base configurations. Table 8 lists the number of successive runs, the number of miss distances less than 5 m, and the capture zone area for the base, minimax, and SA configurations.

The optimization algorithm is implemented on a computer with a Core i7 CPU and 12 GB of RAM. The SA algorithm has an average run time of 79,100 s, while the minimax solver converged in 28,000 s.

## 5. Conclusions

A new approach is proposed for designing the configuration of dual-spin vehicles. This method takes into consideration the practical aspects of structure, aerodynamics, and guidance-control disciplines. A parametric formulation is developed in the structure discipline, which allows for optimal internal layout design as well as optimal external parts of the body. This formulation forms the basis of a Multidisciplinary Design Optimization (MDO) problem in AAO structure. Two algorithms, SA and Minimax, are used to solve the MDO problem. The results indicate that the SA algorithm produces better results compared to the Minimax. However, the CPU time required for the Minimax algorithm is only 0.35 of the SA CPU time. In conclusion, considering a comprehensive set of practical objectives and constraints, the proposed approach yields satisfactory results. Future work will extend this approach by incorporating other MDO approaches.

## Declaration of competing interest

Authors do not have any conflicts of interest to declare.

## References

- [1] Chang S. Dynamic response to canard control and gravity for a dual-spin projectile. *J Spacecraft Rockets* 2016;53(3):558–66. 2016/05/01.
- [2] Seve F, Theodoulis S, Wernert P, Zasadzinski M, Boutayeb M. Flight dynamics modeling of dual-spin guided projectiles. *IEEE Trans Aero Electron Syst* 2017;53(4):1625–41.
- [3] Guan J, Yi W. Modeling of dual-spinning projectile with canard and trajectory filtering. *Int J Aerospace Eng* 2018;2018:7. Article ID 1795158.
- [4] Norris J, Hameed A, Economou J, Parker S. A review of dual-spin projectile stability. *Defence Tech* 2020;16:1–9.
- [5] Burchett B, Peterson A, Costello M. Prediction of swerving motion of a dual-spin projectile with lateral pulse jets in atmospheric flight. *Math Comput Model* 2002;35(7–8):821–34.
- [6] Theodoulis S, Gassmann V, Wernert P, Dritsas I, Kitsios I, Tzes A. Guidance and control design for a Class of spin-stabilized fin-controlled projectiles. *J Guid Control Dynam* 2013;36(2):517–31.
- [7] Wang ZG, Li W. Analysis of free motion characteristics for dual-spin projectile. *Appl Mech Mater* 2013;69–72.
- [8] Zhu D, Tang S, Guo J, Chen R. "Flight stability of a dual-spin projectile with canards " *Proceedings of the Institution of mechanical Engineers. Part G: J Aero Eng* 2015;229(4):703–16.
- [9] Wang Y, Cheng J, Yu J-y, Wang X-m. Influence of yawing force frequency on angular motion and ballistic characteristics of a dual-spin projectile. *Defence Tech* 2016;12(2):124–8. 2016/04/01/.
- [10] Costello M, Peterson A. Linear theory of a dual-spin projectile in atmospheric flight. *J Guid Control Dynam* 2000;23(5):789–97. 2000/09/01.
- [11] Wernert P. Stability analysis for canard guided dual-spin stabilized projectiles." *AIAA atmospheric flight mechanics conference, guidance, navigation, and control and Co-located conferences. American Institute of Aeronautics and Astronautics*; 2009.
- [12] Theodoulis S, Morel Y., Wernert P., and Tzes A., "LPV modeling of guided projectiles for terminal guidance." pp. 1455–1460.
- [13] Theodoulis S, Gassmann V, Brunner T, Wernert P. Robust Bank-to-Turn autopilot design for a class of 155mm spin-stabilized canard-guided projectiles." *AIAA atmospheric flight mechanics (AFM) conference, guidance, navigation, and control and Co-located conferences. American Institute of Aeronautics and Astronautics*; 2013.
- [14] Chang S, Wang Z, Liu T. Analysis of spin-rate property for dual-spin-stabilized projectiles with canards. *J Spacecraft Rockets* 2014;51(3):958–66. 2014/05/01.
- [15] Lee H, Lee CH, Jun BE. Autopilot design for dual-spin projectile based on PI and feedback linearization control. 2014. p. 2084–8.
- [16] Nobahari H, Kermani MA. Integrated optimization of guidance and control parameters in a dual-spin flying vehicle. *Scientia Iranica. Transaction B, Mechanical Engineering* 2017;24(5):2473–89.
- [17] Wang Y, Wang X-m, Yu J-y. Influence of control strategy on stability of dual-spin projectiles with fixed canards. *Defence technology* 2018;14(6):709–19.
- [18] Thai S, Theodoulis S, Roos C, Biannic J-M. Robust design for the roll-channel autopilot of a canard-guided dual-spin projectile. *IFAC-PapersOnLine* 2019;52(12):232–7.
- [19] Zhang Y, Li P., Xiao L., and Tian F., "Research on control scheme of dual-spin projectile with fixed canards." pp. 144–148.
- [20] Jodei J, Ebrahimi M, Roshanian J. Multidisciplinary design optimization of a small solid propellant launch vehicle using system sensitivity analysis. *Struct Multidiscip Optim* 2009;38(1):93–100.
- [21] Yang YR, Jung SK, Cho TH, Myong RS. Aerodynamic shape optimization system of a canard-controlled missile using trajectory-dependent aerodynamic coefficients. *J Spacecraft Rockets* 2012;49(2):243–9.
- [22] Cipd M. MULTI-DISCIPLINARY system design optimization of the F-350 rear suspension. 2004.
- [23] Anderson MB, Burkhalter J, Jenkins R. Missile aerodynamic shape optimization using genetic algorithms. *J Spacecraft Rockets* 2000;37(5):663–9.
- [24] Fu C., Ou Y., Liu J., Yu H., and Xu W., "Adaptive GASA algorithm for multi-disciplinary design optimization." pp. 725–729.
- [25] Şumnu A, Güzelbey İH, Ögücü O. Aerodynamic shape optimization of a missile using a multiobjective genetic algorithm. *Int J Aerospace Eng* 2020;2020.
- [26] Sun X, Ge J, Yang T, Xu Q, Zhang B. Multifidelity multidisciplinary design optimization of integral solid propellant ramjet supersonic cruise vehicles. *Int J Aerospace Eng* 2019;2019.
- [27] Shu HL. Ballistic missile and launch vehicle design. China, BUAA: School of space technology; 2002.
- [28] Han-bing GL-xS, Chun-lin G. Collaborative optimization and its application in the design of space vehicle. *Journal of Projectiles, Rockets, Missiles and Guidance* 2002;S1.
- [29] Balling R, Sobieszcanski-Sobieski J. An algorithm for solving the system-level problem in multilevel optimization. *Struct Optim* 1995;9(3–4):168–77.
- [30] Balling RJ, Sobieszcanski-Sobieski J. Optimization of coupled systems-a critical overview of approaches. *AIAA J* 1996;34(1):6–17.
- [31] Sobieski I., and Kroo I., "Aircraft design using collaborative optimization." p. 715.
- [32] Braun R, Moore A., and Kroo I., "Use of the collaborative optimization architecture for launch vehicle design." p. 4018.
- [33] Alexandrov NM, Lewis RM. Comparative properties of collaborative optimization and other approaches to MDO. 1999.
- [34] Zhang K-s. Concurrent subspace optimization for aircraft system design. *Aeronautics and Astronautics*; 2011. p. 257.
- [35] Sobieszcanski-Sobieski J., Agte J., and Sandusky J., Robert, "Bi-level integrated

- system synthesis (BLISS)." p. 4916.
- [36] Kodyalam S, Sobieszczanski-Sobieski J. Bilevel integrated system synthesis with response surfaces. *AIAA J* 2000;38(8):1479–85.
  - [37] Kim HM, Michelena NF, Papalambros PY, Jiang T. Target cascading in optimal system design. *J Mech Des* 2003;125(3):474–80.
  - [38] Allison J., Walsh D., Kokkolaras M., Papalambros P., and Cartmell M., "Analytical target cascading in aircraft design." p. 1325.
  - [39] Hosseini M, Nosrattollahi M, Sadati H. Multidisciplinary design optimization of UAV under uncertainty. *J Aero Technol Manag* 2017;9:169–78.
  - [40] Czerniak JM, Zarzycki H, Ewald D. AAO as a new strategy in modeling and simulation of constructional problems optimization. *Simulat Model Pract Theor* 2017;76:22–33.
  - [41] Karimi A., Mehrtash M., and Khayat A., "Shape optimization of unguided projectiles using a new multi-objective evolution strategy." p. 912.
  - [42] Lisk D., Robinson T., and Robinson D., "Multi-objective optimization of supersonic projectiles using evolutionary algorithms." p. 1500.
  - [43] Pourtakdoost SH, Mousavi SJ, Jamali S. Multidisciplinary and multi-objective design optimization of a flying projectile using evolutionary algorithm (NSGA-II). *Journal of Aeronautical Engineering* 2014;16(1):17–32 (in persian).
  - [44] Rafique A.F., LinShu H., Zeeshan Q., and Kamran A., "Multidisciplinary design of air-launched space launch vehicle using simulated annealing." pp. 719–726.
  - [45] Zeeshan Q, Yunfeng D, Nisar K, Kamran A, Rafique A. Multidisciplinary design and optimization of multistage ground-launched boost phase interceptor using hybrid search algorithm. *Chin J Aeronaut* 2010;23(2):170–8.
  - [46] Adami A, Mortazavi M, Nosrattollahi M. A new approach in multidisciplinary design optimization of upper-stages using combined framework. *Acta Astronaut* 2015;114:174–83.
  - [47] Zakeri M, Nosrattollahi M, Novinzade A. Multi-disciplinary system design optimization of a launch vehicle upper-stage. *J Aero Technol Manag* 2017;9: 48–62.
  - [48] Vasile JD, Bryson J, Gruenwald BC, Fairfax L, Strohm L, Fresconi F. A multi-disciplinary approach to design long range guided projectiles. 1993.
  - [49] Ranadive T.M., and Baskaran M.M., "An all-at-once CP decomposition method for count tensors." pp. 1–8.
  - [50] Wakayama S, Kroo I. Subsonic wing planform design using multidisciplinary optimization. *J Aircraft* 1995;32(4):746–53.
  - [51] Lambe AB. A matrix-free algorithm for multidisciplinary design optimization. (Canada): University of Toronto; 2015.
  - [52] Arora J, Wang Q. Review of formulations for structural and mechanical system optimization. *Struct Multidiscip Optim* 2005;30(4):251–72.
  - [53] Martins JR, Lambe AB. Multidisciplinary design optimization: a survey of architectures. *AIAA J* 2013;51(9):2049–75.
  - [54] Carlucci DE, Jacobson Sidney S. Ballistics: theory and design of guns and ammunition. third ed. ed. CRC Press; 2007. p. 123–44.
  - [55] Diaz RA, Herrera WJ, Martinez R. Moments of inertia for solids of revolution and variational methods. *Eur J Phys* 2006;27(2):183.
  - [56] Verberne P, Meguid S, Elsayed E. Survivability of embedded microelectronics in precision guided projectiles: modeling and characterization. *Int J Impact Eng* 2021;154:103864.
  - [57] Chakka V, Trabia MB, O'Toole B, Sridharala S, Ladkany S, Chowdhury M. Modeling and reduction of shocks on electronic components within a projectile. *Int J Impact Eng* 2008;35(11):1326–38.
  - [58] Hui J, Gao M, Li X. Dynamic response for shock loadings and stress analysis of a trajectory correcting fuse based on fuse–projectile–barrel coupling. *The Journal of Defense Modeling and Simulation* 2018;15(3):351–64.
  - [59] Herakovich CT. Thin-walled pressure vessels," A concise introduction to elastic solids. Springer; 2017. p. 77–81.
  - [60] Rosema C, Doyle J, Auman L, Underwood M, Blake WB. Missile DATCOM user's manual-2011 revision. Army Aviation and Missile Research Development ENG CTR Redstone Arsenal AL; 2011.
  - [61] Wernert P, Theodoulis S, Morel Y. Flight dynamics properties of 155 mm spin-stabilized projectiles analyzed in different body frames," AIAA atmospheric flight mechanics conference, guidance, navigation, and control and Co-located conferences. American Institute of Aeronautics and Astronautics; 2010.
  - [62] Karimi J R, Reza Mohamad, Hosain Sadati Sayed. Guidance and control of a dual-spin projectile using dynamic inversion method and MRAC-PID controller in cascade structure. *Aerospace Knowledge and Technology Journal* 2021.
  - [63] Ricceri B, Simons S. Minimax theory and applications. Springer Science & Business Media; 2013.
  - [64] Wrobel M. Minimax optimization: without second order information: informatik og matematisk modellering. Danmarks Tekniske Universitet; 2003.
  - [65] Kochenderfer MJ, Wheeler TA. Algorithms for optimization. Mit Press; 2019.
  - [66] McCoy R. Modern exterior ballistics: the launch and flight dynamics of symmetric projectiles. Schiffer Pub.; 1999.